Time-resolved molecular-frame photoelectron angular distributions: Snapshots of acetylene-vinylidene cationic isomerization

N. Douguet,[1] T. N. Rescigno,[2] and A. E. Orel[1]

[1]*Department of Chemical Engineering and Materials Science, University of California, Davis, California 95616, USA*

[2]*Lawrence Berkeley National Laboratory, Chemical Sciences and Ultrafast X-ray Science Laboratory, Berkeley, California 94720, USA*

(Received 21 June 2012; published 30 July 2012)

We report the results of *ab initio* calculations on valence photoionization of the acetylene monocation in its ground (X) and electronically excited (A) states using the complex Kohn variational method. In contrast to the K-shell molecular frame photoelectron angular distributions (MFPADs), which are only sensitive to the molecular geometry, these results show that the valence MFPADs are also sensitive to the electronic state of the target. Hence, the isomerization path from acetylene to vinylidene, which is mediated by a conical intersection responsible for a change in electronic state of the monocation, could, in principle, be traced through valence photoionization.

DOI: 10.1103/PhysRevA.86.013425 PACS number(s): 33.80.Eh

I. INTRODUCTION

Advances in the physics of ultrafast electron and x-ray diffraction have led to experiments where molecular dynamics can be imaged on the time scale of a chemical reaction [1,2]. Such imaging is also possible via photoelectron diffraction when the angular distribution of the photoelectrons are measured in the frame of the molecule [3,4]. In such experiments the molecule must be oriented via three-dimensional laser alignment [5] or the photoelectrons and ion fragments must be measured in coincidence with a momentum imaging technique such as COLTRIMS [6]. In this paper, we present results on molecular frame photoelectron angular distributions (MFPADs) of the acetylene monocation. We show that the shape of the three-dimensional MFPAD is intrinsically connected to the nuclear arrangement and electronic state of the molecular target, implying that changes in the MFPAD can be used to monitor changes in the internal structure of the target in real time.

Here, we consider the example of the isomerization of the low-lying excited state $A\,^2\Sigma_g^+$ of the acetylene monocation $[HCCH]^+$ to the $X\,^2A_1$ vinylidene form $[H_2CC]^+$ or to the acetylene linear ground state $X\,^2\Pi_u$. A COLTRIMS study has been carried out on this process [7] where the heavy particle dissociative fragments were detected in coincidence. The experimentally observed time-of-flight data was interpreted as isomerization via a conical intersection [8]. In our previous study of the K-shell MFPADs for this system [9], it was found that the K-shell MFPADs were only sensitive to photon energy and conformational changes in the target. In the case of the valence MFPADs, we will show that the MFPADs are additionally sensitive to the electronic state of the monocation target. This leads to a more complicated analysis, but has the advantage of specifying the actual energy surface on which the dynamics is taking place on the time scale of the reaction. Since acetylene isomerization occurs via a conical intersection near an equilibrium trans-bent geometry (C_{2h}) with strong vibronic couplings resulting in a change of electronic state, the valence MFPADs yield an additional level of information compared to the K-shell MFPADs.

In the next section, we present a brief description of the theoretical methods used to calculate the MFPADs. Section III describes our structure calculations and the obtained isomerization paths on the two relevant X and Aelectronic states of $HCCH^+$, corresponding, respectively, to the ground and first excited plane-symmetric states. In Sec. IV, we present MFPADs calculated at a few geometry points on the isomerization paths and at different photoelectron energies. We discuss the main features of the valence photoionization of acetylene monocation and the expected effects of these in an experimental measurement. Finally, the results and potential applications are discussed in the last section.

II. THEORETICAL APPROACH

In order to determine a photoionization cross section, the following matrix elements, expressed in terms of body-frame amplitudes, are needed:

$$I^{\mu}_{\Gamma_o l_o m_o} \equiv \langle \Psi_o | \mu \left| \Psi^-_{\Gamma_o l_o m_o} \right\rangle = \sum_{i=1}^{N} \int \Psi_o(r_1, r_N) r_i^{\mu} \Psi^-_{\Gamma_o l_o m_o}(r_1, r_N) d^3 r_1 \cdots d^3 r_N, \tag{1}$$

where the function Ψ_o represents the initial state of the target molecule, r^{μ} is the dipole operator defined in the length form as

$$r^{\mu} = \begin{cases} z, & \mu = 0 \\ \mp(x \pm iy)/\sqrt{2}, & \mu = \pm 1, \end{cases} \tag{2}$$

and $\Psi^-_{\Gamma_o l_o m_o}$ is the continuum state describing the scattering of an electron, with angular momentum quantum numbers l_o, m_o from, in this case, the final dication in quantum state Γ_o.

We use the complex Kohn variational method [10,11] to describe the scattering of an electron from the acetylene dication. In the Kohn method, the final wave function representing the electron-ion scattering, with the ion in a state Γ_o, is expressed as

$$\Psi^-_{\Gamma_o l_o m_o} = \sum_{\Gamma} \hat{A}\left(\chi_{\Gamma} F^-_{\Gamma\Gamma_o}\right) + \sum_i d_i^{\Gamma_o} \Theta_i, \tag{3}$$

 ©2012 American Physical Society

where the first sum runs over energetically open ionic states described by $(N-1)$-electron wave functions χ_Γ and the second sum runs over N-electron configuration-state functions Θ_i representing penetration and correlation terms. The operator $\hat{A}$ ensures antisymmetrization of the wave function.

In the Kohn method, the functions $F^-_{\Gamma\Gamma_o}$ are expanded as

$$F^-_{\Gamma\Gamma_o} = \sum_i c_i^{\Gamma\Gamma_o}\phi_i(r) + \sum_{lm}[f_l(k_\Gamma,r)\delta_{ll_o}\delta_{mm_o}\delta_{\Gamma\Gamma_o} + T^{\Gamma\Gamma_o}_{ll_omm_o}h^-_l(k_\Gamma,r)]Y_{lm}(\hat{r})/r, \quad (4)$$

where f_l and h^-_l are partial-wave continuum radial functions, behaving asymptotically as regular and incoming Coulomb functions ($Z=2$), and ϕ_i is a set of square integrable (Cartesian-Gaussian) functions.

The matrix element in Eq. (1) is combined in a partial-wave series,

$$I_{\hat{k}_{\Gamma_o},\hat{\epsilon}} = \sqrt{\frac{4\pi}{3}}\sum_{l_om_o\mu} i^{l_o}e^{-i\delta_{l_o}}I^\mu_{\Gamma_o}Y^*_{1\mu}(\hat{\epsilon})Y^*_{l_om_o}(\hat{k}_{\Gamma_o}), \quad (5)$$

to construct an amplitude representing an ejected electron with momentum $\boldsymbol{k}_{\Gamma_o}$, associated with a particular ion channel and a direction of light polarization $\hat{\epsilon}$. The doubly differential cross section for a hypothetical space-fixed target molecule is then given as

$$\frac{d^2\sigma^{\Gamma_o}}{d\Omega_{\hat{k}}d\Omega_{\hat{\epsilon}}} = \frac{8\pi\omega}{3c}\left|I_{\hat{k}_{\Gamma_o},\hat{\epsilon}}\right|^2, \quad (6)$$

where c is the speed of light and ω represents the photon energy.

As was recently shown [12], it is particularly useful to consider the differential body-frame quantity obtained by integrating the above doubly differential cross section over all directions of photon polarization $\hat{\epsilon}$. Using Eqs. (6) and (5), and the orthonormality of the spherical harmonics $Y^*_{1\mu}(\hat{\epsilon})$, the following expression is easily derived:

$$\int\frac{d^2\sigma^{\Gamma_o}}{d\Omega_{\hat{k}}d\Omega_{\hat{\epsilon}}}d\Omega_{\hat{\epsilon}} = \frac{32\pi^2\omega}{9c}\sum_\mu\left|\sum_{l_om_o}I^\mu_{\Gamma_o}Y_{l_om_o}(\hat{k}_{\Gamma_o})\right|^2. \quad (7)$$

If we denote an MFPAD over a specific component μ of the dipole operator by $M^\mu_{\Gamma_o}(\hat{k})$, then the cross section in Eq. (7) is simply the incoherent sum over dipole operator components, namely,

$$\int\frac{d^2\sigma^{\Gamma_o}}{d\Omega_{\hat{k}}d\Omega_{\hat{\epsilon}}}d\Omega_{\hat{\epsilon}} = \frac{32\pi^2\omega}{9c}\sum_\mu\left|M^\mu_{\Gamma_o}(\hat{k})\right|^2. \quad (8)$$

In the case of nondegenerate electronic states, the above quantity is symmetric under any operation of the irreducible representation of the initial target molecular point group. In the case of degenerate electronic states, this quantity must be summed over degenerate states to obtain a meaningful physical quantity that ultimately exhibits the molecular symmetry. For a molecule with one heavy atom, such as methane, with tetrahedral symmetry, the polarization-averaged MFPAD should be symmetric under any operation of the $T_d(M)$ group. However, this fact does not necessarily imply that the MFPAD images the actual shape of the molecule and the chemical bonds. In fact, for K-shell photoionization of methane, it was found that over a range of low photoelectron energies, the MFPAD reproduces the four C–H bonds, that is, the electron preferably scatters along the bond directions [12]. The same effect was found for water and ammonia [13]. It is reasonable to ask whether the same "molecular imaging" would be found in targets with more than one heavy atom. In the case of a molecule with more than one heavy atom, the possibility of multiple interference phenomena exist. In our recent study of K-shell photoionization of acetylene monocation [9], we found the integrated MFPADs to show, in addition to the expected structure, "ghost structures" opposite to the C–H bond directions. We speculated that this could be attributed to multiple scattering effects in the case of a target with more than a single heavy atom. We now have reason to believe that this effect has more to do with the lack of charge neutrality in a target ion than it does with multiple scattering [14]. In any case, we will show in Sec. IV that although the valence MFPADs do not simply image the target monocation in the present case, they nevertheless give conformational information about the different C–H bonds. All of the MFPADs we will present below will be the polarization-averaged quantities defined in Eq. (8).

III. STRUCTURE CALCULATIONS AND REACTION PATHS

At its linear equilibrium geometry, the electronic configuration of neutral acetylene is $1\sigma_g^2 1\sigma_u^2 2\sigma_g^2 2\sigma_u^2 3\sigma_g^2 1\pi_u^4$. Through photoionization, an electron can be removed from either a $1\pi_u$ orbital to form the $^2\Pi_u$ ground state of acetylene, or from the $3\sigma_g$ orbital to form the $^2\Sigma_g^+$ first excited state of acetylene. Once the molecule distorts without torsion, the point group of the molecule is reduced to C_s. Hence, the degenerate $^2\Pi_u$ state splits into an A' state with configuration $5a'^2 6a' 1a''^2$ and an A'' state with configuration $5a'^2 6a'^2 1a''$, while the excited $^2\Sigma_g^+$ state has A' symmetry with configuration $5a'6a'^2 1a''^2$. Since the critical part of the isomerization process, namely, a nonadiabatic transition, occurs through the two A' states (commonly referred to as X and A, respectively), we restrict our consideration to dynamics on these two states.

In order to describe the isomerization mechanism undergone by excited $[HCCH]^+$ following photoionization of the neutral species, we determined the relevant minimum-energy paths (MEPs) of the reaction. The first set of calculations were performed using the MOLPRO suite of codes [15] to determine the MEPs and equilibrium positions through the quadratic steepest descent (QSD) method [16]. We first performed a state-averaged multiconfiguration self-consistent field (MCSCF) calculation to obtain an orbital basis for a more extensive multireference configuration-interaction (MRCI-1) expansion. For the latter, we doubly occupied the two carbon $1s$ orbitals, chose a complete active space of eight additional orbitals, and included all single excitations outside the complete active space, which results in expansions of about one million configurations.

The reaction paths on both X and A energy surfaces were determined for the relevant initial and final configurations of $C_2H_2^+$. The calculated X and A electronic energies along these paths are plotted in Fig. 1 as a function of the path length $s = \int ds$, where $ds^2 = \sum dx_i^2$ measures the total nuclear

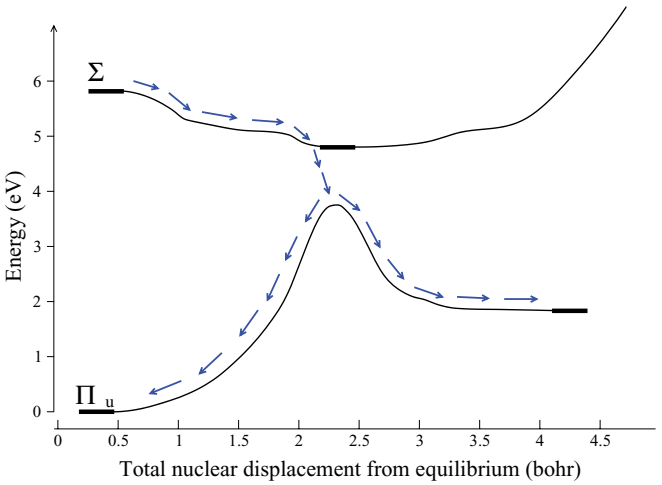

FIG. 1. (Color online) Electronic energy of the acetylene monocation X and A states as a function of the reaction path length. The isomerization path from the excited $^2\Sigma_g^+$ state of acetylene towards either the vinylidene $^2A_1$ state or the $^2\Pi_u$ acetylene ground state is schematically represented by arrows. The origin of energies is taken at the acetylene $^2\Pi_u$ ground state.

displacement. The isomerization of acetylene monocation is represented schematically by blue arrows in the figure. Assuming the A state of the monocation is populated by photoionization of neutral acetylene, the starting geometry is chosen to be the linear equilibrium geometry of the neutral molecule. However, the minimum energy on the A state surface lies at a bent, planar, trans-symmetric geometry (^2A_g). At this minimum, the X and A states are separated by approximately 1 eV. The nonadiabatic coupling between the X and A states is large in this region, as there is a conical intersection between them at a nearby trans-symmetric geometry [17,18]. Therefore, the system undergoes a nonadiabatic transition onto the X state, where the trans-bending configuration is a saddle point, which potentially leads to either vinylidene ($^2A_1$) or acetylene ($^2\Pi_u$) monocations, with a slightly steeper descent towards the $^2\Pi_u$ ground state. We note that there is also a local minimum on the A state surface in a vinylidene configuration, but the large potential barrier required to reach it makes it irrelevant to the present study. For clarity, we do not show the A'' component of the potential surface in Fig. 1 that originates from the splitting of the $^2\Pi_u$ degenerate state. We note that nonadiabatic transitions from the X to the A'' state, leading to the $^2\Pi_u$ state, should be rather slow on the time scale of the nuclear dynamics along the A' states, since a torsion of the molecule is necessary. Thus, for simplicity, we will not consider photoionization from this antisymmetric state.

The energies and equilibrium geometries of the $^2\Pi_u$, $^2A_1$, and ^2A_g electronic states of acetylene monocation are given in Table I, where the C–H and C–C bond distances are, respectively, denoted R_{CH} and R_{CC}, and θ represents the C-C-H angle. Also shown in the table are the initial geometry and energy of the $^2\Sigma_g^+$ state, taken at the linear equilibrium position of neutral acetylene [19]. The MRCI-1 results are compared with other extensive *ab initio* calculations from Refs. [18,19] and an overall very good agreement is observed.

The scattering calculations must of necessity be carried out with simpler target electronic states. For this reason, we performed a second set of MRCI calculations (MRCI-0) using the same molecular orbital basis, but with no excitations outside the complete active reference space. Therefore, the preliminary MRCI-1 calculation is not only used to find the correct reaction path and equilibrium positions, but also serves as a reference calculation. We have indeed verified that the potential curves calculated with MRCI-0 behave as predicted by the MRCI-1 calculation, and that the corresponding electronic energies in Table I are in relatively good agreement with the more precise calculations. As can be seen from the table, the MRCI-0 $^2\Sigma_g^+$ and ^2A_g state relative energies agree with the MRCI-1 energies to better than 10%. The observed difference is slightly larger for the $^2A_1$ state. However, we found that the shape of the MFPADs is relatively insensitive to changes in the wave function such as the number of active orbitals used to determine the target states, as long as the electronic excitations can be represented inside the reference space and a reasonable agreement in energy exists. Indeed, we have also carried out calculations with a smaller reference space and verified that although the agreement in energy is worse, the changes in the shape of the MFPADs were negligible. The results of $C_2H_2^+$ photoionization are discussed in detail in the next section.

TABLE I. Calculated equilibrium geometries and relative energies of the ^2A_g, $^2\Pi_u^+$, and $^2A_1$ states. Also shown are the initial geometry and energy of the excited $^2\Sigma_g^+$ state, taken at the equilibrium geometry of neutral acetylene. All relative energies are given with respect to the acetylene $^2\Pi_u$ ground state. CCSD(T) represents coupled-cluster theory with single, double, and partially triple excitations.

Elec. states	Method	Taken from	R_{CH} (Å)	R_{CC} (Å)	θ (deg)	ΔE (eV)
$^2\Pi_u(D_{\infty h})$	MRCI-1 (MRCI-0)	This work	1.077	1.254	180.0	0 (0)
	MRCI	Ref. [18]	1.082	1.259	180.0	0
	CCSD(T)	Ref. [19]	1.079	1.255	180.0	0
$^2A_1(C_{2v})$	MRCI-1 (MRCI-0)	This work	1.099	1.280	118.5	1.86 (2.36)
	MRCI	Ref. [18]	1.096	1.281	119.0	1.87
	CCSD(T)	Ref. [19]	1.102	1.280	118.5	1.89
$^2A_g(C_{2h})$	MRCI-1 (MRCI-0)	This work	1.171	1.288	107.1	4.76 (5.28)
	MRCI	Ref. [18]	1.171	1.283	108.0	4.79
	CCSD(T)	Ref. [19]	1.175	1.288	106.9	4.80
$^2\Sigma_g^+(D_{\infty h})$	CCSD(T)	Ref. [19]	1.064	1.210	180.0	
	MRCI-1 (MRCI-0)	This work				5.80 (5.94)

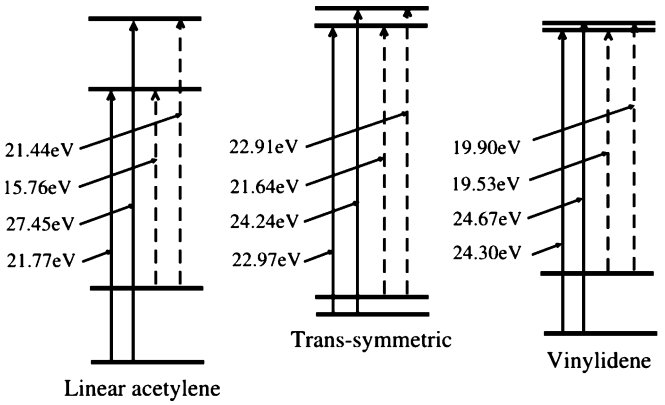

FIG. 2. Ionization energies from the X and A electronic states of $C_2H_2^+$, to the $\widetilde{X}$ and $\widetilde{A}$ electronic states of $C_2H_2^{++}$. Energies are given, in eV, at the three characteristic geometries: linear acetylene, trans-symmetric, and vinylidene. Solid and dashed arrows represent, respectively, photoionization from the X and A states.

IV. RESULTS

The isomerization of the acetylene monocation involves three characteristic conformations of the molecule, namely, the linear acetylene equilibrium geometry, the trans-symmetric saddle-point geometry, and the vinylidene equilibrium geometry. The different ionization energies, determined from our MRCI-0 structure calculations, represent an important characteristic of the photoionization process and are presented at each geometry in Fig. 2. We have used the notation $\widetilde{X}$ and $\widetilde{A}$ to refer to the ground and first excited states, respectively, of the dication. These states are nominally described by removing either a $6a'$ or a $5a'$ electron, respectively, from the $(5a'^2 6a' 1a''^2)$ X state of the monocation. We note that the $\widetilde{A}$ state is doubly degenerate at linear geometries, where the $6a'$ and $1a''$ orbitals are degenerate. It is interesting to note the following points from the figure: First, the ionization energies at different geometries are rather close, remaining less than 3 eV apart. The particular case of the linear $A \mapsto \widetilde{X}$ transition represents the only exception, but the latter transition is of minor importance since its associated photoionization cross section is small. Indeed, this transition represents a second-order process; its cross section would actually be identically zero in a single configuration approximation, since it requires a two-electron transition and the dipole operator is a one-electron operator.

At constant photon energy along the path, the photoelectron energies and the corresponding MFPADS span a small portion of the energy spectrum. Actually, on the reaction path from the trans-symmetric configuration to the vinylidene ground state, the photoelectron energies remain almost constant and only photoionization at near linear configurations have higher photoelectron energies. Moreover, the dication channels become close to one another at trans-symmetric and vinylidene geometries, such that the second dication channel is open even at low electron energies. In fact, although not shown in the figure, a low-lying third channel $(5a'^0 6a'^2 1a''^2)$ is also open at low energy in the vinylidene configuration and was therefore included in our calculations at all geometries. Finally, although not shown in the figure, it is worth noting that the ionization energies at the starting linear geometry on the A state are similar to the ones of the linear acetylene ground state.

As already discussed in Sec. II, the polarization-averaged MFPADs, when summed over all degenerate final channels, reflect the symmetry of the initial target state and may potentially image the molecular bonds. For this reason, it is interesting to study the changes in the form of the MFPADs at the important geometries of the molecular monocation through its isomerization path. We recently applied this procedure to study the K-shell photoionization of $C_2H_2^+$ [9], where a clear dependence of the MFPAD on conformational changes and photoelectron energies was observed, although the C–H bonds were not simply imaged. At a given photoelectron energy, the corresponding MFPADs from K-shell photoionization are only sensitive to changes in nuclear geometry. The situation is dramatically different in valence photoionization from either the X or A states, since an electron can be removed from different types of initial orbitals. Let us take the example of photoionization to the $\widetilde{A}$ state $(5a'6a')$ of the dication. The photoionization event $X \mapsto \widetilde{A}$ from the X state $(5a'^2 6a')$, and the photoionization event $A \mapsto \widetilde{A}$ from the A state $(5a'6a'^2)$, correspond to the removal of an electron from either the $6a'$ or the $5a'$ orbitals, respectively, so observable changes between both MFPADS are expected. We also expect differences in the MFPADs for the $X \mapsto \widetilde{X}$ and $A \mapsto \widetilde{X}$ transitions, although the latter has a small photoionization cross section, as explained previously.

In order to illustrate the discussion, we first present the MFPADs at the linear equilibrium position of the monocation. Since the isomerization of acetylene was described over the entire reaction path through the C_s group, we calculated the MFPADs at a slightly bent geometry (less than 1°) from the true linear equilibrium position. In this way, we

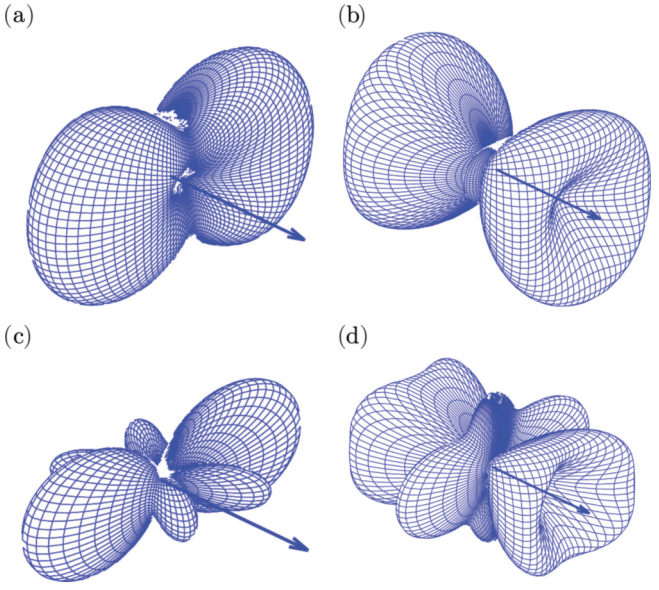

FIG. 3. (Color online) Polarization-averaged valence MFPADs at acetylene linear geometry for a photoelectron energy of 0.5 eV. The panels correspond to (a) $X \mapsto \widetilde{X}$, (b) $A \mapsto \widetilde{X}$, (c) $A \mapsto \widetilde{A}$, and (d) $X \mapsto \widetilde{A}$ photoionizations. The arrows lie along the C–C axis and their lengths give the magnitude of the cross section in units of kb/sr. 1 kb $= 10^{-21}$ cm^2. Arrow lengths are (a) 8, (b) 1, (c) 2, and (d) 7.

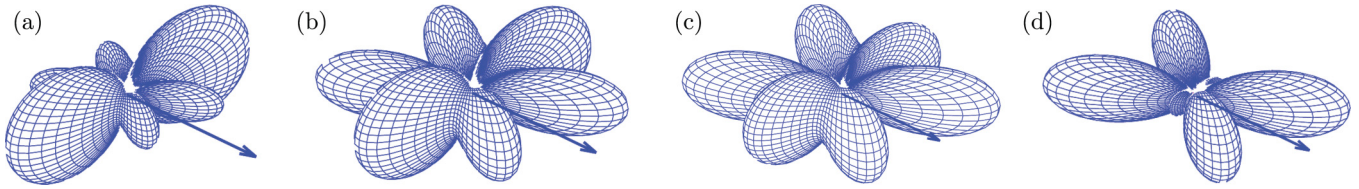

FIG. 4. (Color online) Change of the valence MFPAD in $A \mapsto \widetilde{A}$ photoionization with increasing photoelectron energy. The panels (a)–(d) correspond, respectively, to 0.5, 1, 2, and 3 eV photoelectron energy. Arrow lengths are 1.5 kb/sr at all energies.

lift any degeneracies and can study photoionization between A' symmetric states only, as we are mostly interested in the form and changes of the MFPAD along the reaction path for a single photoionization transition. The MFPADs for the low-lying photoionization transitions, at a small photoelectron energy (0.5 eV), are plotted in Fig. 3. The arrows in each MFPAD indicate the C–C bond direction. Figure 3(a) corresponds to $X \mapsto \widetilde{X}$ photoionization, for which the photoelectron preferential directions belong, for the main part, to the plane orthogonal to the orientation of the chemical bonds. Notice that the MFPAD has C_{2v} symmetry, but does not have infinite rotational symmetry along the C–C axis. As explained in Sec. II, this fact is understood since we only considered photoionization from the A' state and did not add the contribution from the degenerate (in linear geometry) A'' electronic state. Indeed, it is clear from Fig. 3(a) that one would get a rotationally symmetric picture by simply adding to the current MFPAD, an MFPAD rotated by 90°. The situation is different for the $A \mapsto \widetilde{X}$ transition in Fig. 3(b), which exhibits clearly the rotational symmetry, because it corresponds to a transition between nondegenerate Σ states. The $A \mapsto \widetilde{A}$ and $X \mapsto \widetilde{A}$ transitions have a more complicated structure. Here, in order to obtain averaged rotationally symmetric MFPADs, the MFPADs corresponding to all transitions between the doubly degenerate initial and final states must be included. It is clear from the results shown in Fig. 3 that the MFPADs, even at the low value of photoelectron energy chosen, are quite sensitive both at the initial and final electronic state.

It is also interesting to track changes in the valence photoionization MFPADs as the photoelectron energy increases. The results for the $A \mapsto \widetilde{A}$ transition are plotted in Fig. 4. Changes in the preferential scattering directions are evident. The lobes perpendicular to the C–C axis become smaller as the photoelectron energy increases towards 3 eV. Above 3 eV, the shape of the MFPAD does not change appreciably. We do not show corresponding results for the $X \mapsto \widetilde{X}$ transition since they do not change appreciably as the energy increases. Clearly, above 3 eV, the MFPADs for the $X \mapsto \widetilde{X}$ and the $A \mapsto \widetilde{A}$ transitions are different.

We next consider other conformations along the reaction path, starting from the trans-symmetric geometry. At this conformation, the MFPADs exhibit C_{2h} symmetry. In Fig. 5, the MFPADs for $X \mapsto \widetilde{X}$ and $A \mapsto \widetilde{A}$ photoionization are given

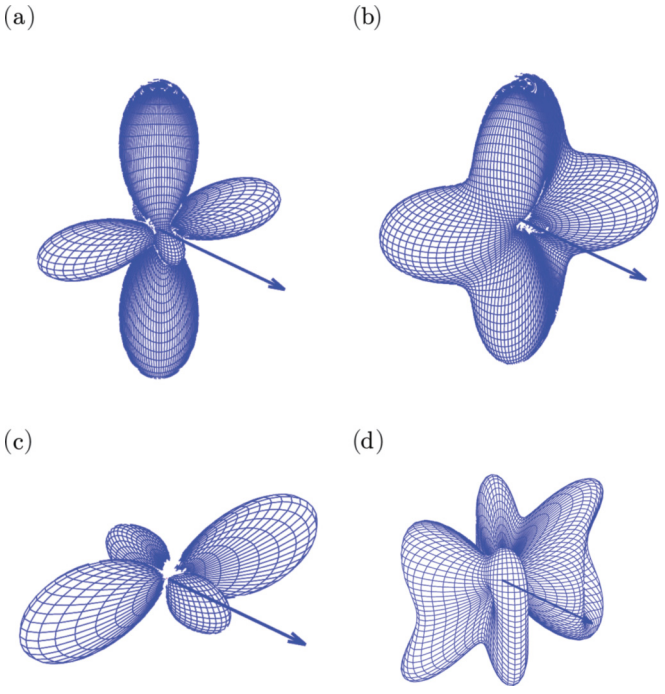

FIG. 5. (Color online) Polarization-averaged valence MFPADs at trans-symmetric geometry. The panels (a) and (c) correspond to $X \mapsto \widetilde{X}$ photoionization and the panels (b) and (d) correspond to $A \mapsto \widetilde{A}$ photoionization. Upper panels: photoelectron energy is 0.5 eV; lower panels: photoelectron energy is 6 eV. Arrow lengths, in kb/sr, are (a) 45, (b) 6, (c) 85, and (d) 3.

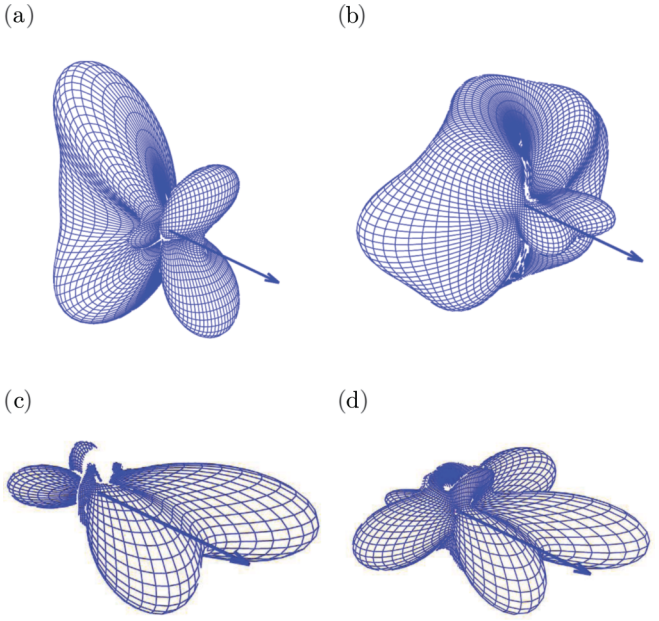

FIG. 6. (Color online) Polarization-averaged valence MFPADs at vinylidene geometry. The panels (a) and (c) correspond to $X \mapsto \widetilde{X}$ photoionization and the panels (b) and (d) correspond to $X \mapsto \widetilde{A}$ photoionization. Photoelectron energy is (a) 0.5, (b) 0.5, (c) 5, and (d) 8 eV. Arrow lengths, in kb/sr, are (a) 22, (b) 8, (c) 35, and (d) 15.

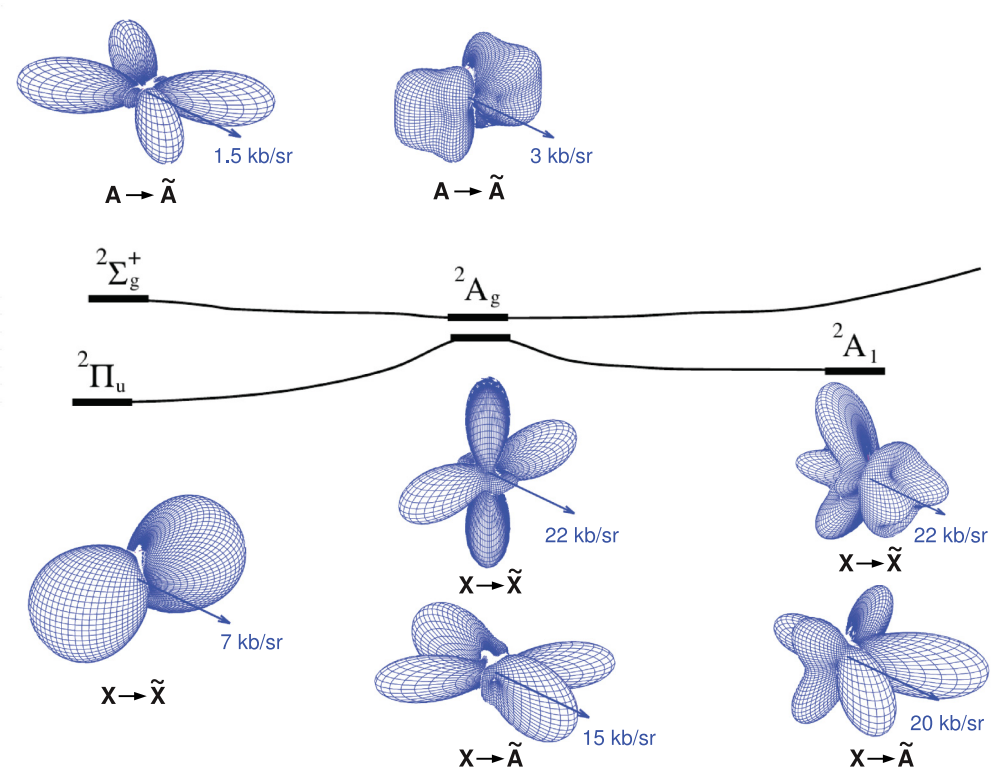

FIG. 7. (Color online) Reaction path and corresponding MFPADs at the important conformations of acetylene monocation.

at two different photoelectron energies. At low photoelectron energy (0.5 eV), the MFPADs for both transitions are similar, but bear little resemblance in shape to the target cation and show preferential directions for electron ejection perpendicular to the C–C axis. At the higher energy shown, the MFPADs do show dominant electron ejection at angles close to 70° with respect to the C–C bond, which is close to the orientation of the C–H bonds in trans-symmetric geometry, as well as smaller "ghost" lobes. We note that at high photoelectron energy, the cross section for $X \mapsto \widetilde{X}$ photoionization is more than an order of magnitude larger than the $A \mapsto \widetilde{A}$ photoionization cross section. The $X \mapsto \widetilde{X}$ cross section at this geometry is also significantly larger than it is at linear geometry. Concerning the $X \mapsto \widetilde{A}$ transition, we have found that although the main scattering directions belong to the molecular plane, the MFPADs do not resemble the actual conformation of the molecule.

We now turn to the study of the vinylidene ground-state equilibrium position, which represents a possible final rearrangement of the molecule through isomerization of the excited acetylene monocation. As explained in Sec. III, there is no need to consider photoionization from the A state near the vinylidene geometry. At the vinylidene conformation, we have found complicated shapes for the MFPADs and observed strong variations with the photoelectron energy. Some relevant MFPADS are shown in Fig. 6 for both transitions and at different energies. Figures 6(a) and 6(b) show MFPADs at 0.5 eV photoelectron energy for the $X \mapsto \widetilde{X}$ and $X \mapsto \widetilde{A}$ transitions, respectively. Evidently, the MFPADs at the vinylidene geometry do not image the bonds at low energy. Indeed, for the $X \mapsto \widetilde{X}$ transition in Fig. 6(a), the electron scatters in the plane perpendicular to the molecular plane, while for the $X \mapsto \widetilde{A}$ transition shown in Fig. 6(b), electron ejection is predominantly in-plane but opposite to the direction of the C–H chemical bonds. For the higher photoelectron energies shown in Figs. 6(c) and 6(d), the predominant direction of ejection shifts toward the hydrogen side of the cation for both transitions, but the overall shapes of the MFPADs do not image the target.

We close with a visualization of the MFPADs for the dominant valence ionization processes at the three discussed geometries along the isomerization path. The results are for a fixed photon energy of 25.5 eV and are shown in Fig. 7. Note that at this photon energy, the $X \mapsto \widetilde{A}$ channel is closed at linear geometry. At the vinylidene geometry, only transitions from the X state are shown, since the A state cannot be populated by photoisomerization, as discussed above. Although there are clearly changes in the MFPADs along the path to isomerization, the shapes do not necessarily reflect the geometry changes in a clear way. It is perhaps most noteworthy to point out that the magnitude of the cross sections for both $X \mapsto \widetilde{X}$ and $X \mapsto \widetilde{A}$ are large at the trans-symmetric geometry, while the $A \mapsto \widetilde{A}$ cross sections remain relatively small. Therefore, when the system nonadiabatically passes to the X state, changes in the angular distributions would be accompanied by a sudden increase in the photoionization cross section, which should be detectable.

V. DISCUSSION

We have considered the isomerization of the excited acetylene monocation, using MFPADs to track changes along the reaction path. In contrast to our earlier study of this system

using core-level MFPADs to monitor the reaction, the present study considered MFPADs from valence photoionization. We have found that the valence angular distributions, in addition to being sensitive to geometric changes in the molecular target cation, also depend strongly on the initial and final electronic states involved. While this dependence lends an additional level of richness to the expected angular distributions, in practice it may seriously complicate the interpretation of observable data.

There are some aspects of the particular example studied here that could hinder an experimental study. In the present case, two photoionization steps are required, one to first ionize the neutral acetylene into an excited monocation state and another to ionize the monocation. The pump step would produce a strong background of low-energy photoelectrons, which might complicate the detection of a weaker population of photoelectrons, with comparable energies, arising from the probe step. Moreover, the fact that the electronic energy surface of the excited A state is relatively flat means that an initially localized nuclear wave packet could spread rapidly, thereby complicating the identification of a specific final geometry. Ideally, one might prefer to experiment with cases where the pump step is nonionizing and launches a wave packet on a steeply dissociative electronically excited surface. The ethylene molecule presents such an example and will be the subject of a future study.

ACKNOWLEDGMENTS

This work was performed under the auspices of the US Department of Energy by LBNL under Contract No. DE-AC02-05CH11231 and was supported by the US Department of Energy Office of Basic Energy Sciences, Division of Chemical Sciences.

[1] A. H. Zewail *et al.*, Science **328**, 187 (2010).
[2] H. Chapman *et al.*, Nature (London) **470**, 73 (2010).
[3] Y. Arasaki, K. Takatsuka, K. Wang, and V. McKoy, J. Chem. Phys. **132**, 124307 (2010).
[4] P. Hockett, C. Z. Bisgaard, O. J. Clarkin, and A. Stolow, Nature Phys. **7**, 612 (2011).
[5] J. L. Hansen *et al.*, Phys. Rev. A **83**, 023406 (2011).
[6] R. Dorner *et al.*, Phys. Rep. **330**, 95 (2000).
[7] Y. H. Jiang *et al.*, Phys. Rev. Lett. **105**, 263002 (2010).
[8] M. E. Madget, O. Vendrell, and R. Santra, Phys. Rev. Lett. **107**, 263002 (2011).
[9] T. Rescigno, N. Douguet, and A. E. Orel [J. Phys. B (to be published)].
[10] C. W. McCurdy and T. N. Rescigno, Phys. Rev. A **39**, 4487 (1989).
[11] A. E. Orel, T. N. Rescigno, and B. H. Lengsfield, Phys. Rev. A **44**, 4328 (1991).
[12] J. B. Williams *et al.*, Phys. Rev. Lett. **108**, 233002 (2012).
[13] C. S. Trevisan, C. W. McCurdy, and T. N. Rescigno [J. Phys. B (to be published)].
[14] N. Douguet, T. Rescigno, and A. E. Orel (unpublished).
[15] H. J. Werner, P. J. Knowles, G. Knizia, F. R. Manby, M. Schütz *et al.*, computer code MOLPRO, version 2010.1 (2010), http://www.molpro.net.
[16] J. Sun and K. Ruedenberg, J. Chem. Phys. **101**, 2157 (1994).
[17] P. Rosmus, P. Botschwina, and J. P. Maier, Chem. Phys. Lett. **84**, 71 (1981).
[18] G. Chambaud, R. Van den Boom, and P. Rosmus, Chem. Phys. Lett. **247**, 79 (1995).
[19] S. Boyé-Péronne and D. Gauyacq, J. Chem. Phys. **124**, 214305 (2006).